The Astrophysical Journal Letters, 959:L28 (12pp), 2023 December 20 https://doi.org/10.3847/2041-8213/ad0ed8

A Primordial Origin for the Gas-rich Debris Disks around Intermediate-mass Stars

Riouhei Nakatani[1,2], Neal J. Turner[1], Yasuhiro Hasegawa[1], Gianni Cataldi[3], Yuri Aikawa[4], Sebastián Marino[5], and Hiroshi Kobayashi[6]
[1] NASA Jet Propulsion Laboratory, California Institute of Technology, 4800 Oak Grove Drive, Pasadena, CA 91109, USA; ryohei.nakatani@jpl.nasa.gov
[2] RIKEN Cluster for Pioneering Research, 2-1 Hirosawa, Wako-shi, Saitama 351-0198, Japan
[3] National Astronomical Observatory of Japan, Osawa 2-21-1, Mitaka, Tokyo 181-8588, Japan
[4] Department of Astronomy, Graduate School of Science, The University of Tokyo, Tokyo 113-0033, Japan
[5] Department of Physics and Astronomy, University of Exeter, Stocker Road, Exeter, EX4 4QL, UK
[6] Department of Physics, Nagoya University, Furo-cho, Chikusa-ku, Nagoya, Aichi 464-8602, Japan
Received 2023 July 14; revised 2023 November 21; accepted 2023 November 22; published 2023 December 20

Abstract

While most debris disks consist of dust with little or no gas, a fraction have significant amounts of gas detected via emission lines of CO, ionized carbon, and/or atomic oxygen. Almost all such gaseous debris disks known are around A-type stars with ages up to 50 Myr. We show, using semianalytic disk evolution modeling, that this can be understood if the gaseous debris disks are remnant protoplanetary disks that have become depleted of small grains compared to the interstellar medium. Photoelectric heating by the A stars' far-UV (FUV) radiation is then inefficient, while the stars' extreme-UV (EUV) and X-ray emissions are weak owing to a lack of surface convective zones capable of driving magnetic activity. In this picture, it is relatively difficult for stars outside the range of spectral types from A through early B to have such long-lived gas disks. Less-massive stars have stronger magnetic activity in the chromosphere, transition region, and corona with resulting EUV and X-ray emission, while more-massive stars have photospheres hot enough to produce strong EUV radiation. In both cases, primordial disk gas is likely to photoevaporate well before 50 Myr. These results come from 0D disk evolution models where we incorporate internal accretion stresses, MHD winds, and photoevaporation by EUV and X-ray photons with luminosities that are functions of the stellar mass and age. A key issue this work leaves open is how some disks become depleted in small dust so that FUV photoevaporation slows. Candidates include the grains' growth, settling, radial drift, radiation force, and incorporation into planetary systems.

Unified Astronomy Thesaurus concepts: Protoplanetary disks (1300); Debris disks (363); Stellar evolution (1599); Extreme ultraviolet astronomy (2170); Exoplanet formation (492); Interstellar medium (847); A stars (5)

1. Introduction

A fundamental goal of planet formation research is to learn the evolutionary pathways that protoplanetary disks (PPDs) follow to become planetary systems and their associated debris disks. Classically, the PPD lifetime is estimated to be no longer than 10 Myr based on near- and mid-infrared (IR) observations that trace the inner hot dust ($\lesssim$1–10 au; Haisch et al. 2001; Hernández et al. 2007; Meyer et al. 2007; Mamajek 2009; Ribas et al. 2014, 2015) and ultraviolet (UV) and Hα observations tracing accreting gas (e.g., Kennedy & Kenyon 2009; Fedele et al. 2010; Sicilia-Aguilar et al. 2010). Thus, 10 Myr is considered a typical timescale on which gas-rich PPDs evolve into gas-free debris disks.

An explanation is therefore needed for the more than 20 gaseous debris disks observed around stars older than 10 Myr (e.g., Kóspál et al. 2013; Lieman-Sifry et al. 2016; Marino et al. 2016; Higuchi et al. 2017; Hughes et al. 2017; Moór et al. 2017; Higuchi et al. 2019a, 2019b; Kral et al. 2020). Two hypotheses have been proposed for the origins of this gas. In the primordial-origin scenario, the gas is a remnant of the PPD. In the secondary-origin scenario, the gas was released more recently from volatiles in planetesimals associated with the dust in the debris disks.

While the secondary-origin scenario has been extensively examined through modeling (Kral et al. 2016, 2019; Matrà et al. 2019; Moór et al. 2019; Cataldi et al. 2020; Marino et al. 2020, 2022), less attention has been paid to the primordial-origin scenario (Nakatani et al. 2021; Smirnov-Pinchukov et al. 2022; Iwasaki et al. 2023). A primordial origin has been considered unlikely because of the short canonical PPD gas disk lifetime. However, hydrodynamical modeling by Nakatani et al. (2021) shows that if the PPD around an intermediate-mass star ($M_* \approx 2\,M_\odot$) is depleted in submicron grains, including polycyclic aromatic hydrocarbons (PAHs), then the photoelectric heating produced when far-UV (FUV) photons strike the grains is weak enough to slow photoevaporation so the gas could survive well past 10 Myr and into the debris disk stage; with efficient FUV photoevaporation, the gas lifetimes are most likely $\lesssim$10 Myr regardless of stellar masses (Komaki et al. 2023; Ronco et al. 2023). Primordial origins thus have the potential to account for the occurrence of gaseous debris disks around A stars (Lieman-Sifry et al. 2016; Moór et al. 2017; Hughes et al. 2018).

The outstanding questions include what gas lifetimes to expect quantitatively in the primordial-origin scenario, how these depend on the stellar mass, and whether the results are consistent with the observed occurrence rates of gaseous debris disks. We address these issues here by constructing disk evolution models using a semianalytic 0D approach.

2. Overall Picture of Gas Disk Evolution

Theoretical works indicate that the gas disks are dispersed by accretion onto the central star (Shakura & Sunyaev 1973; Lynden-Bell & Pringle 1974) and by ejection in winds, launched either by magnetic forces (e.g., Suzuki & Inutsuka 2009; Bai & Stone 2013a, 2013b) or by photoevaporation (e.g., Shu et al. 1993; Hollenbach et al. 1994; Richling & Yorke 1998). These three processes' relative importance varies over the course of disk evolution; accretion and/or magnetohydrodynamic (MHD) winds dominate the mass loss in the early stage, when the disk is relatively massive, while photoevaporation dominates later, when the disk mass decreases to $\lesssim 10^{-2}\,M_\odot$ at ages of 1–10 Myr (e.g., Clarke et al. 2001; Gorti et al. 2015; Carrera et al. 2017; Kunitomo et al. 2020, 2021; Komaki et al. 2023; Weder et al. 2023).

This picture of time-varying disk dispersal processes is consistent with several observational facts. For instance, class 0/I jets have much larger mass-loss rates (10^{-7}–$10^{-6}\,M_\odot\,\mathrm{yr}^{-1}$) than photoevaporation can provide, implying that the ejection is driven by MHD effects in these early stages. For another example, the luminosity of a photoevaporative wind tracer, the [Ne II] 12.8 μm low-velocity component, is higher for more evolved disks, i.e., slow accretors ($\sim 10^{-8}\,M_\odot\,\mathrm{yr}^{-1}$) and inner dust-depleted disks (Pascucci et al. 2020).

Jet and wind mass-loss rates in the upper end of the range imply possibly enough material crossing the lines of sight between star and disk to block much of the stellar UV and X-ray radiation. This can slow or stop the disk's photoevaporation (for a recent review, see Pascucci et al. 2023). In 3D MHD modeling by Takasao et al. (2022), the outflow from the disk around a solar-mass star has a column density high enough to attenuate the UV and X-ray photons at accretion rates $\gtrsim 10^{-8}\,M_\odot\,\mathrm{yr}^{-1}$. Overall, a fairly advanced age and low rates of accretion and outflow appear necessary before photoevaporation can dominate gas disk dispersal.

3. Gas Lifetime Estimate

For the primordial-origin hypothesis to be a possible scenario, one of the critical necessary conditions PPDs must meet is to retain a mass reservoir beyond 10 Myr, especially at outer radii ($\gtrsim$1–10 au) where gaseous debris disks are detected. This study's primary objective is to demonstrate its feasibility, as it was previously considered implausible. Our model will be tailored for this purpose, as will be described below. We focus on the disks where PAHs and small grains ($\lesssim 0.01\,\mu$m) are depleted compared to the interstellar medium (ISM). These are the systems that potentially meet the necessary condition; otherwise, the disks dissipating through rapid photoelectric heating most likely have short lifetimes of <10 Myr (Gorti et al. 2009, 2015; Komaki et al. 2021, 2023); we ignore this population. Thus, we here derive the lifetime for the subpopulation of PPDs where the gas is the longest-lived. The estimated lifetime is distinct from the average gas lifetime, which depends on the still-unknown probability of achieving a small grain–depleted state.

We do not specify here the processes responsible for grain depletion. Instead, we simply assume the disks reach a small grain–depleted state before photoevaporation begins to dominate disk dispersal, regardless of the stellar mass. Several effects can deplete the dust, especially for intermediate-mass stars. Grain growth and radial drift reduce the local dust-to-gas ratio (e.g., Sellek et al. 2020). The drift is likely especially rapid around young intermediate-mass stars (Pinilla et al. 2022). The intense radiation force from intermediate-mass stars can also blow out small dust (Owen & Kollmeier 2019; Nakatani et al. 2021).

The specific level of small-grain depletion needed to inhibit FUV photoevaporation remains uncertain. Nakatani et al. (2018a, 2018b) explored FUV photoevaporation varying disk metallicity and demonstrated that strong FUV photoevaporation demands a small-grain abundance exceeding $\sim$0.1%–1% of the ISM level. However, these investigations focus on a $0.5\,M_\odot$ star with extremely high FUV luminosity, lowering the oxygen and carbon abundances with metallicity, which limits the results' general applicability. The critical small-grain abundance depends on stellar mass and FUV/X-ray luminosities, yet prior studies explored a limited parameter space. Further investigations are warranted. Nevertheless, it is likely that critical small-grain abundances exist, below which FUV photoevaporation becomes negligible. We anticipate this threshold to be around $\sim$0.1%–1% of the ISM level, following Nakatani et al. (2018a, 2018b).

Observations suggest that the PAH abundance in PPDs is at least 10 times less than the interstellar value (e.g., Geers et al. 2007; Oliveira et al. 2010; Vicente et al. 2013). The hybrid disk HD 141569A is depleted to a level where photoelectric heating may drive only weak photoevaporation (Li & Lunine 2003; Thi et al. 2014). Nondetection of PAHs occurs with a reasonable fraction in Herbig disks, where the detection rate is $\sim$70% (e.g., Acke et al. 2010), or in T Tauri disks, where it is $\lesssim$10% (e.g., Geers et al. 2006). Such nondetection hints at abundances potentially over 100 times lower than interstellar levels. This significant depletion in the disk atmosphere is also indicated from mid-IR spectra (e.g., Furlan et al. 2006, 2011) and implied from IR scattered-light imaging (e.g., Mulders et al. 2013). These findings lead us to infer that these disks might be in the small grain–depleted state.

3.1. Semianalytic Model

Our model employs a 0D approach, following the disk's mass decrease from accretion and wind mass loss in the early stage and from photoevaporation in the late stage. It is based on the analytic lifetime estimate from the UV-switch model (Clarke et al. 2001; detailed in Appendix A). In that model, the major dispersal process is viscous accretion at the early stage and switches to photoevaporation beginning at the "switching time," t_0, which defines the transition point into the late stage. Thereafter, it disperses the remaining disk mass of $M'_{\mathrm{disk},0}$. This model returns t_0, $M'_{\mathrm{disk},0}$, and the gas disk lifetime $t_{\mathrm{life,g}}$ analytically (see Equations (A5)–(A7)) once the disk mass $M_{\mathrm{disk}}(t)$ (see Equation (A4)) and photoevaporation rate $\dot{M}_{\mathrm{ph}}(t)$ are given as functions of time.

The original UV-switch model uses purely viscous disks, but here we consider disks evolving under angular momentum and mass extraction through a magnetically driven wind alongside the internal angular momentum redistribution by turbulent stresses. Observational evidence that PPDs appear to evolve by driving magnetized winds is discussed by Rafikov (2017), Manara et al. (2022), and Pascucci et al. (2023). We adopt the analytic disk evolution model of Chambers (2019) for $M_{\mathrm{disk}}(t)$, as set out in Appendix B. We first derive t_0 and $M'_{\mathrm{disk},0}$ by finding the time when the disk mass loss $\dot{M}_{\mathrm{disk}}(t)$ and photoevaporation rates $\dot{M}_{\mathrm{ph}}(t)$ are equal; we will define

$\dot{M}_{\rm ph}(t)$ later. $t_{\rm life,g}$ is then the time until the remaining mass is photoevaporated, found by numerically integrating

$$M_{\rm disk}(t=t_0) = M'_{\rm disk,0} = \int_{t_0}^{t_{\rm life,g}} dt\ \dot{M}_{\rm ph}(t).$$

The resulting $t_{\rm life,g}$ is insensitive to the choice of the threshold mass to define "dispersal," as $M_{\rm disk}$ falls rapidly after $t=t_0$. The disk's initial mass is taken as proportional to the stellar mass with $M_{\rm disk,0}=0.1\ M_*$ (e.g., Williams & Cieza 2011; Andrews et al. 2013; however, a steeper scaling, $\propto M_*^{1.3-2.0}$, is found by Ansdell et al. 2016, 2017; Pascucci et al. 2016; see Manara et al. 2022 for a recent review). We explore $t_{\rm life,g}$'s dependence on $M_{\rm disk,0}$ and the scaling in Appendix D.

Photoevaporation is generally driven by FUV, extreme-UV (EUV), and X-ray radiation. However, as stated above, we here consider only cases where FUV grain photoelectric heating is negligible, and the photoevaporative winds are driven solely by the EUV and X-ray heating associated with photoionization. We also assume that the disks are isolated from massive stars, so external photoevaporation is negligible. We use the EUV photoevaporation rate estimate

$$\dot{M}_{\rm EUV} = 4.1\times10^{-10}\,M_\odot\ {\rm yr}^{-1}\left(\frac{\Phi_{\rm EUV}}{10^{41}\ {\rm s}^{-1}}\right)^{1/2}\left(\frac{M_*}{1\ M_\odot}\right)^{1/2} \quad (1)$$

(Hollenbach et al. 1994; Clarke et al. 2001), since it agrees well with the mass-loss rates derived by radiation hydrodynamics simulations (Nakatani et al. 2021). Based on 1 + 1D modeling, EUV photoevaporation rates were thought to increase about tenfold after the disk center was cleared out, letting the stellar EUV field dominate over the diffuse EUV from recombining ions. However, 2D axisymmetric radiative transfer showed that the direct stellar component dominates even in disks without central cavities (Tanaka et al. 2013). Additionally, radiation hydrodynamics modeling found no significant difference in photoevaporation rates with and without cavities of various sizes (Owen et al. 2010; Picogna et al. 2019; Nakatani et al. 2021). Hence, we apply the Equation (1) photoevaporation rates uniformly throughout disk evolution.

The stellar EUV emission rate $\Phi_{\rm EUV}$ can be decomposed into photospheric, chromospheric ($\sim10^4$ K), transition regional ($\sim10^5$ K), and coronal ($\sim10^6$ K) components. We shall refer to the last three jointly as magnetic-origin EUV, $\Phi_{\rm EUV,mag}$. For the photospheric EUV component, we use Kunitomo et al.'s (2021) Table 1 results from long-term stellar evolution calculations for $0.5\,M_\odot \leqslant M_* \leqslant 5\,M_\odot$. We estimate the magnetic-origin EUV emission rate from the X-ray luminosity $L_{\rm X}$ using the $\Phi_{\rm EUV}$–$L_{\rm X}$ relation of Shoda & Takasao (2021),

$$\log\left(\frac{\Phi_{\rm EUV,mag}}{1\ {\rm s}^{-1}}\right) = 20.40 \ + \ 0.66\log\left(\frac{L_{\rm X}}{1\ {\rm erg\ s}^{-1}}\right). \quad (2)$$

Strictly, this relation applies to solar-type stars, but we apply it to all the stars considered here ($0.5\,M_\odot \leqslant M_* \leqslant 5\,M_\odot$). Since the theoretical and observational uncertainties in $\Phi_{\rm EUV,mag}$ are large, we believe this estimate is a reasonable first-order approximation.

We follow Kunitomo et al. (2021) for $L_{\rm X}$ time evolution, excluding the $L_{\rm X}/L_* = 10^{-7}$ floor applied to intermediate-mass stars in the original paper. We expect the floor not to apply universally, given that most Herbig stars do not present X-ray emissions detected at this level (e.g., Hamaguchi et al. 2005; Stelzer et al. 2006). Instead, we employ $L_{\rm X} = \min(10^{-3.13},\ 5.3\times10^{-6}Ro^{-2.7})L_*$, where Ro represents the Rossby number (Mangeney & Praderie 1984; Noyes et al. 1984) defined as ${\rm Ro} = P_{\rm rot}/\tau_{\rm conv}$, with $P_{\rm rot}$ and $\tau_{\rm conv}$ being the rotational period and convective turnover timescale. Kunitomo et al. (2021) set $P_{\rm rot}$ to 3 days and calculate $\tau_{\rm conv}$ from the stellar evolution model. The rotational period can range between 1 and 10 days in general, but the qualitative trend in the time evolution of $L_{\rm X}$ is independent of $P_{\rm rot}$ (see Section 5.2 of Kunitomo et al. 2021). Thus, the variation of $P_{\rm rot}$ would have a limited impact on our results. The total EUV emission rate is $\Phi_{\rm EUV} = \Phi_{\rm EUV,ph} + \Phi_{\rm EUV,mag}$. We omit accretion-generated EUV and X-ray here but address their influence on $t_{\rm life,g}$ in Appendix C.

Stellar/interstellar Lyman–Werner (LW) radiation-driven photoevaporation might be important for small grain–depleted disks around stars with $2\,M_\odot \lesssim M_* \lesssim 3\,M_\odot$ (hereafter late intermediate-mass stars). However, our radiation hydrodynamics simulations indicate that LW photoevaporation is negligible even for late intermediate-mass stars (R. Nakatani et al. 2024, in preparation). Thus, we do not consider LW photoevaporation in this study. The dependence of LW photoevaporation on stellar mass and luminosity is currently unknown but warrants investigation in future research.

For X-ray photoevaporation, the mass-loss rate is still under debate. Some studies obtained large mass-loss rates (Ercolano et al. 2009; Owen et al. 2010; Picogna et al. 2019), while others found weaker mass loss (Gorti et al. 2009; Wang & Goodman 2017; Nakatani et al. 2018b; Komaki et al. 2021). The different conclusions likely originate from the adopted X-ray spectra, where mass-loss rates are high if the spectrum has a certain level of soft X-rays ($\sim$0.1 keV; Ercolano et al. 2009; Gorti et al. 2009; Nakatani et al. 2018b; Sellek et al. 2022); the incorporated cooling processes, where the studies with large X-ray photoevaporation rates neglect important cooling processes; and the adopted numerical methods. To cover the uncertainty of X-ray photoevaporation rates, we estimate the lifetimes with and without X-ray photoevaporation.

For X-ray photoevaporation rates, we use the formula of Owen et al. (2012):

$$\dot{M}_{\rm X} = 4.8\times10^{-9}\,M_\odot\ {\rm yr}^{-1}\left(\frac{L_{\rm X}}{10^{30}\ {\rm erg\ s}^{-1}}\right)^{1.14}\left(\frac{M_*}{1\ M_\odot}\right)^{-0.148}. \quad (3)$$

(Using the formula of Picogna et al. 2019 instead results in very similar lifetimes.) Given the disagreement over X-ray photoevaporation rates discussed above, Equation (3) must be considered an upper limit, so the corresponding $t_{\rm life,g}$ is a lower limit. The total photoevaporation rate is

$$\dot{M}_{\rm ph} = \begin{cases} \dot{M}_{\rm EUV} & ({\rm w/o\ X-ray\ photoevaporation}) \\ \max\left(\dot{M}_{\rm EUV},\ \dot{M}_{\rm X}\right) & ({\rm w/\ X-ray\ photoevaporation}) \end{cases}.$$

We calculate the lifetimes for two cases: (i) EUV-only and (ii) EUV + X-ray with Equations (1) and (3). In Appendix E, we additionally discuss how the observed spread in $L_{\rm X}$ (e.g., Güdel et al. 2007) can affect $t_{\rm life,g}$. Note that using the sum instead of $\max\left(\dot{M}_{\rm EUV},\ \dot{M}_{\rm X}\right)$ does not make a difference, as $\dot{M}_{\rm X}$ dominates $\dot{M}_{\rm EUV}$ significantly.

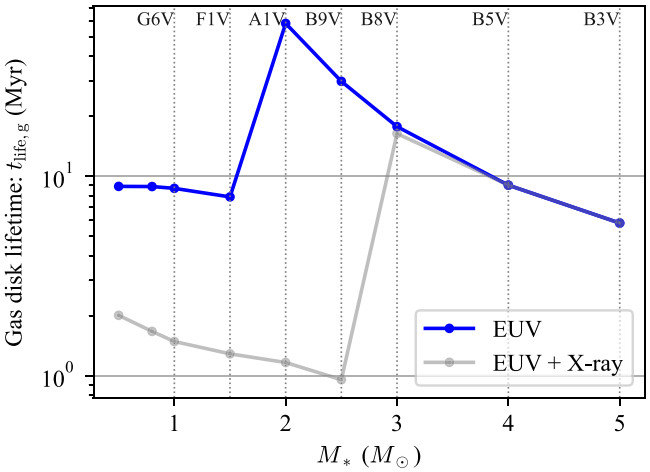

Figure 1. Estimated gas disk lifetime $t_{\rm life,g}$ as a function of M_*. The blue line indicates $t_{\rm life,g}$ for the EUV-only case. The gray line adds X-ray photoevaporation. The spectral type corresponding to each M_* is presented on the top axis. Note that these lifetimes apply only to small grain–depleted disks and not to disks where FUV photoelectric heating drives photoevaporation.

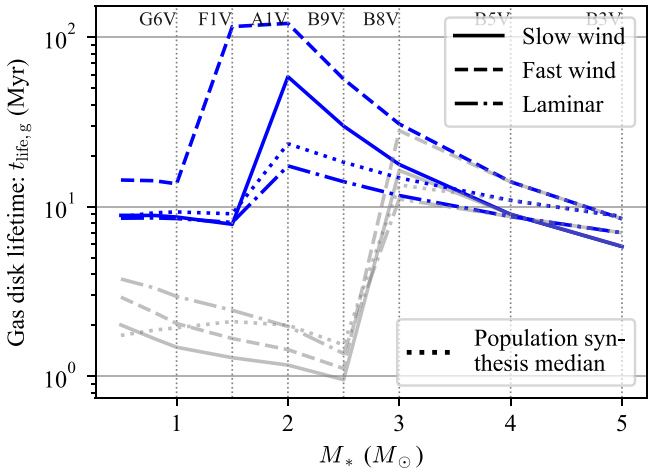

Figure 2. Same axes as Figure 1. Solid, dashed, and dotted–dashed lines show lifetimes of slow-wind, fast-wind, and laminar disks, respectively. The dotted lines show the median lifetimes of the population synthesis in Appendix D.

3.2. Results

To provide an overview, we start with Figure 1, the estimated $t_{\rm life,g}$ as a function of M_* using the Chambers (2019) model for disks dominated by slow winds. Here the accretion is predominantly driven by the wind, which also extracts a significant fraction of the disk's mass (see Section 4.3 of the original paper for details). The figure shows the corresponding spectral type at each M_* determined by $T_{\rm eff}$ when the stars reach the zero-age main-sequence (ZAMS) in the table of Kunitomo et al. (2021). The relation between the spectral type and $T_{\rm eff}$ is taken from Pecaut & Mamajek (2013). The table of Kunitomo et al. (2021) ends before stars with $M_* \leqslant 1\,M_\odot$ reach the ZAMS. Thus, for $M_* = 1\,M_\odot$, we used the last $T_{\rm eff}$ value in the table to determine the spectral type; the spectral types of $M_* < 1\,M_\odot$ stars are undetermined and thus not specified in Figure 1.

In the EUV-only case (blue), the lifetime peaks at $M_* = 2\,M_\odot$ or, equivalently, spectral types around A0. Lifetimes longer than 10 Myr are found only around the late intermediate-mass stars ($2\,M_\odot \lesssim M_* \lesssim 3\,M_\odot$), corresponding to spectral types between F0 and B8. The surface convective zones of these stars disappear at ∼1–10 Myr, and the magnetic-origin EUV emission is already weak by the time photoevaporation comes to dominate mass loss. The results indicate that primordial gas disks relatively easily survive to the ages of young debris disks around A- and late B-type stars.

Stars with $M_* \geqslant 4\,M_\odot$ (hereafter early intermediate-mass stars) produce much stronger photospheric EUV emission owing to their high $T_{\rm eff}$, leading to shorter $t_{\rm life,g}$. For stars of solar mass and below, the magnetic-origin EUV emission remains strong throughout the disk dispersal.

X-ray photoevaporation (gray line in Figure 1) reduces the lifetime by 1–2 orders of magnitude for $\lesssim 3\,M_\odot$ compared to the EUV-only case. This is because $L_{\rm X}$ is kept high at $\gtrsim 10^{31}$ erg s^{-1}, corresponding to $\dot{M}_{\rm X} \sim 5 \times 10^{-8}$–$10^{-7}\,M_\odot$ yr^{-1}, until the disk completely disperses. However, as mentioned above, the adopted X-ray photoevaporation rates might be overestimated. While X-ray photoevaporation can explain observational wind diagnostics (e.g., Weber et al. 2020; Rab et al. 2022), such high X-ray photoevaporation rates are also known to be unfavorable for explaining the observed disk mass and accretion rates with viscous disk models (Sellek et al. 2020; Alexander et al. 2023) and magnetized disk models (Weder et al. 2023); smaller mass-loss rates as EUV photoevaporation alone are preferred. However, we do not rule out the effectiveness of X-rays in driving photoevaporation, as they indeed deposit energy to the gas but with somewhat smaller mass-loss rates than Equation (3). If so, the lifetimes of the EUV models set upper limits for low-mass stars. For the early intermediate-mass stars ($\geqslant 4\,M_\odot$), $t_{\rm life,g}$ matches the EUV-only case, since the convective zone disappears before 1 Myr.

We then explore the dependence on the parameters of the MHD wind-driven accretion and mass loss across the fast-wind and laminar disk regimes in Chambers (2019). In the fast-wind case, the wind mass loss is negligible, and most of the accretion is driven by the wind, while in the laminar case, wind mass loss is substantial, and the wind drives almost all of the accretion (Sections 4.2 and 4.4 of the original paper). The resulting $t_{\rm life,g}$–M_* relation (Figure 2) is essentially the same as in Figure 1, consistently peaking at $2\,M_\odot$. Small differences are that in the fast-wind model, $t_{\rm life,g}$ at $1.5\,M_\odot$ becomes comparable to $2\,M_\odot$, and in the laminar model, the peak lifetime at $2\,M_\odot$ is reduced to ∼20 Myr. However, the assumption of no wind mass loss in the fast-wind model seems difficult to reconcile with the high detection rate of the [O I] λ6300 low-velocity component (∼80%; Nisini et al. 2018), making it an unfavored PPD evolution scenario. The stellar mass–dependent trends are consistent across a wide parameter space, as shown by the population synthesis median in Figure 2 (see Appendix D). Overall, varying the disk and wind parameters yields a wide range of possible lifetimes, especially near $1.5\,M_\odot$. We conclude that the average lifetime peaks at early A-type stars with $t_{\rm life,g} > 10$ Myr for small grain–depleted disks.

We emphasize that the lifetimes derived here apply only to small grain–depleted disks. Figures 1 and 2 neglect any short-lived disks that might be dispersed by FUV photoevaporation. To quantify the general frequency of gas disks, it would be necessary to estimate the PPDs' probability of becoming depleted in small grains. This is an issue for future studies.

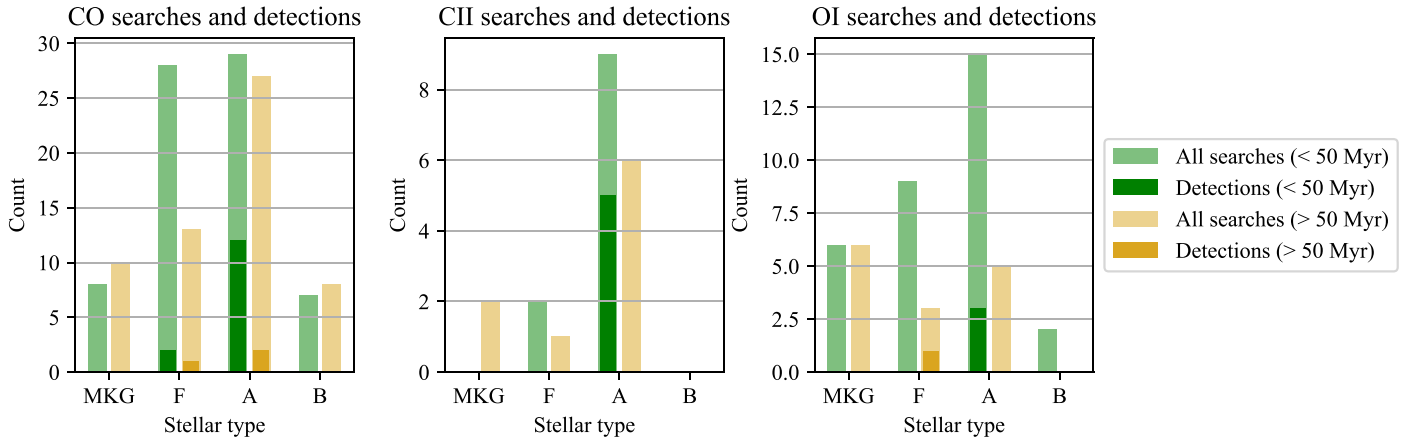

Figure 3. Detection rates of gaseous debris disks are highest among young A-type stars. The tracers are CO millimeter emission (left), C II 157 μm (middle), and O I 63 μm (right). The light green histograms show the all-survey count and are superposed by dark green histograms indicating the detection count for sources younger than 50 Myr. The light and dark yellow histograms are sources older than 50 Myr. The horizontal axis gives the stellar type. Integrated counts are shown for M, K, and G stars. All data are from Hughes et al.'s (2018) Table 1. These trends are consistent with the M_*-dependence of our predicted lifetimes in Figure 1.

We attribute the stellar mass dependence of $t_{\rm life,g}$ mostly to the variation with M_* in the EUV and X-ray luminosities and thus the photoevaporation rates. However, the variation of MHD effects with stellar mass may also play a role. The hard X-rays from low-mass stars ($\lesssim 1\,M_\odot$) can ionize the disk atmosphere to increase the local effective α. This enhances the MHD winds' effects, shortening the disk lifetime. The soft X-rays due to shocks originating from line-driven winds of early B- and O-type stars could have a similar effect and can also directly drive soft X-ray photoevaporation. Both of these effects would strengthen the gas lifetime difference between the late intermediate-mass stars and the rest.

Currently, no evidence supports the presence of companions in known gas-rich debris disks, but the possibility still remains that they could harbor unseen low-mass, close-in companions. In these scenarios, the EUV and X-ray emission may be dominated by these companions, boosting photoevaporation rates. Thus, to yield long-lived gas disks, late intermediate-mass stars should not have such companions.

4. Comparison with Detection Rates of Gaseous Debris Disks

We now compare the modeled lifetimes from Section 3 with the population of debris disks detected in the CO millimeter, [C II] 157 μm, or [O I] 63 μm lines, focusing on the dependence on host star spectral type. The detections come from Supplemental Table 1 of Hughes et al. (2018). Only 3 out of 152 sources listed in the table have ages of $<$10 Myr, with all being A0 stars. The age of HD 166191 (F star) is presented as 4 Myr, but we adopt an updated value of $\sim$10 Myr (Potravnov et al. 2018; Su et al. 2022). As they discussed, this sample combines studies with diverse sensitivity limits and selection criteria and thus is not well suited for determining quantitative occurrence rates. However, the spectral-type dependence resembles that in a more uniform sampling by Moór et al. (2017).

Keeping this limitation in mind, we replot the detections compiled by Hughes et al. (2018) versus stellar type in Figure 3. We show not only the detections in CO but also those in C II and O I, since the disks may retain these species mixed with hydrogen even in the absence of CO. We note that 9 of 12 young CO-detected sources have CO mass $M_{\rm CO} > 10^{-4}\,M_\oplus$ (see Table A1 of Moór et al. 2017, 2019; Marino et al. 2020). The three sources below this threshold are likely better explained by secondary origins, based on the short photodissociation lifetimes for primordial CO at such low gas masses. For F stars, one of the two young CO-detected sources is above this mass threshold and is early F (F2/3V); the one below the threshold is late F (F5/6V). The decreasing trend of the incidence from A to FGK stars is likely real but not due to a sensitivity bias. A comparison of debris disks with similar fractional luminosities (Tables A1 and A2 of Marino et al. 2020) indicates that only two out of nine sources exhibit gas (at levels $\lesssim 10^{-4}\,M_\oplus$) among FGK stars, while 11 out of 17 A-type stars display a gas presence (often exceeding $10^{-3}\,M_\oplus$).

Figure 3 shows several interesting consistencies with the modeled $t_{\rm life,g}$–M_* relation. The detection rate is highest for early A-type stars (more than half the stars with gas detected are early A-type, A0–A3). Almost all of the gas-rich debris disks with $M_{\rm CO} > 10^{-3}\,M_\oplus$ are hosted by early A-type stars. The exception is HD 121191 ($3 \times 10^{-3}\,M_\oplus$; Moór et al. 2017), which is type A5 but does not necessarily disagree with our model considering the range in $t_{\rm life,g}$ at $M_* \sim 1.5\,M_\odot$. Our model naturally explains younger ($<$50 Myr) gaseous debris disks' higher numbers around A-type stars than around both lower-mass and O and early B stars. The decreasing trend toward higher-mass stars could be due to both photoevaporation and intense CO photodissociation. For A stars, the weak photodissociating fluxes would also be helping the long survival of CO. Overall, within the limitations of the sample, the consistencies with the model are remarkable.

In contrast, the gas detected in debris disks around late F stars appears more compatible with secondary origins, given the short gas lifetime around those low-mass stars in our model. Also, a few debris disks have multiple lines of evidence supporting a secondary origin, among them the A5–A6 star β Pic (e.g., Dent et al. 2014; Greaves et al. 2016; Cataldi et al. 2023; Iwasaki et al. 2023). We thus consider primordial and secondary origins not mutually exclusive. We stress that our hypothesized disk evolution does not necessarily rule out a secondary origin for some gaseous debris disks, even among A-type stars younger than 50 Myr. Determining the gas origins in individual sources is a challenge for the future. However, the results we present here suggest that the high overall frequency

of gas-rich debris disks among A-type stars can come from a primordial origin.

5. Summary and Outlook

The substantial amounts of gas found in some debris disks could either be remnants of the primordial PPD or originate in the secondary release of volatiles from bodies resembling comets or asteroids. While the primordial-origin scenario was classically considered unlikely, here we demonstrated that primordial gas can survive to the ages of the known gaseous debris disks, using semianalytic models to derive lifetimes for the gas in disks that have been depleted in small grains ($\lesssim$0.01 μm) so that FUV photoelectric heating is ineffective. The resulting lifetimes are longest around stars of $2\,M_\odot \lesssim M_* \lesssim 3\,M_\odot$, whose evolution switches off their surface convection at 1–10 Myr before the disk loses the bulk of its gas. Without a surface convective zone, these stars lack surface magnetic activity and thus have low luminosities in the EUV and X-ray bands that drive the photoevaporation of the gas.

The gas lifetime consistently exceeds 10 Myr for the late intermediate-mass stars only. The shorter lifetimes of the gas disks around lower-mass stars ($\lesssim 1\,M_\odot$) are due to strong EUV and X-rays from the chromosphere, transition region, and corona, while those around higher-mass stars ($\gtrsim 4\,M_\odot$) are due to the high photospheric temperatures and resulting EUV luminosities.

Our model predicts a higher frequency of gaseous debris disks around A- and late B-type stars compared to types both earlier and later. This is qualitatively consistent with the observed population, motivating further investigation of the primordial-origin scenario. Longer gas disk lifetimes for A stars could be a factor in the giant planet occurrence rate peaking at 1.7–1.9 $M_\odot$ (Reffert et al. 2015; Wolthoff et al. 2022), though more detailed modeling of the dissipating disks would be needed to assess the possibility of gas giant formation (see also Johnston et al. 2023, for a recent model). Likewise, our results could relate to the increasing occurrence of transition disks with stellar mass (van der Marel & Mulders 2021). Further investigations are needed to evaluate whether these transition disks might serve as precursors to gaseous debris disks.

The primordial-origin picture allows the existence around late intermediate-mass stars of long-lived gas-rich disks with very weak dust emission, which we term "phantom" disks. Finding such phantom disks would indicate that the abundant CO gas in at least some young debris disks is primordial. Searches for gas-rich, dust-poor disks, especially around A and late B stars aged 10–50 Myr, could thus help determine the range of evolutionary paths followed by planet-forming disks. Note that the phantoms are different from the relic disks, purely viscous, dusty disks with central cavities larger than 100 au surviving >10 Myr around solar-type stars owing to very weak X-ray emission (Owen et al. 2011).

The fraction of PPDs achieving the small grain–depleted state and the critical level of depletion required to inhibit FUV photoevaporation are open questions. Further hydrodynamics investigations are needed considering a range of stellar masses and FUV/X-ray luminosities. We anticipate that PPDs with PAH/small-grain abundances below ~0.1%–1% of the interstellar level (see Section 3) may have reached this state and could be potential precursors of gas-rich debris disks around intermediate-mass stars. PPDs with PAH/small-grain abundances above the critical level might have FUV-driven, slow H_2 winds extending to ~10–100 au with temperatures exceeding a few hundred K and mass-loss rates of $\sim 10^{-9}$–$10^{-8}\,M_\odot\,\mathrm{yr}^{-1}$ (Nakatani et al. 2018a, 2018b; Komaki et al. 2021). Searching for these molecular winds could also help examine the depletion level in PPDs and very young (<10 Myr) hybrid disks (e.g., HD 141569), including hybrid disk candidates (Iglesias et al. 2023), around weak X-ray emitters.

The point of this work is that gas disks can persist beyond 10 Myr, a necessary condition for the primordial-origin scenario. A caveat is that our 0D approach cannot unambiguously predict the detailed surface density evolution and the alignment with other observational characteristics of inner disks, such as accretion and wind mass-loss rates (Appendix F). Comparison with these observables would help assess the feasibility of the proposed evolutionary pathways. Our future 1D simulations will accurately follow the radial profile evolution, enabling us to make such comparisons. Nevertheless, we expect the conclusion on the long lifetimes around intermediate-mass stars will remain consistent even in more advanced models, as the key determinant of outer gas disk lifetimes, which potentially manifest as gaseous debris disks in observations, is the photoevaporation rates set by the stellar emission rates. The speed of final-stage disk dispersal would not be significantly influenced by how the inner disks clear. Thermochemical modeling would also help in understanding how the CO and C masses evolve in small grain–depleted disks and examine if the final values reproduce observations (Cataldi et al. 2023; Iwasaki et al. 2023). For a broader perspective, it is worth investigating what fraction of PPDs in general can be long-lived considering environmental factors like external photoevaporation, tidal truncation, and late infall.

Acknowledgments

We are grateful to the anonymous referees for the useful comments. We thank Masanobu Kunitomo and Akimasa Kataoka for their practical and insightful comments on this study. R.N. is supported by the Japan Society for the Promotion of Science (JSPS), Overseas Research Fellowship. S.M. is supported by a Royal Society University Research Fellowship (URF-R1-221669). This research was performed in part at the Jet Propulsion Laboratory, California Institute of Technology, under contract 80NM0018D0004 with the National Aeronautics and Space Administration and with the support of the NASA Exoplanets Research Program through grant 17-XRP17_2-0081. This work strongly benefited from the Core2disk-III residential program of Institut Pascal at Université Paris-Saclay, with the support of the program "Investissements d'avenir" ANR-11-IDEX-0003-01.

Software: Numpy (Harris et al. 2020), Matplotlib (Hunter 2007), Astropy (Astropy Collaboration et al. 2013, 2018, 2022), SciPy (Virtanen et al. 2020)

Appendix A
The UV-switch Model

The evolution of an accretion disk redistributing its angular momentum via viscous friction can be described by

$$\frac{\partial \Sigma}{\partial t} = \frac{3}{R}\frac{\partial}{\partial R} R^{1/2} \frac{\partial}{\partial R} \nu \Sigma R^{1/2} \tag{A1}$$

(Lynden-Bell & Pringle 1974). If the disk evolves purely viscously with the viscosity profile of $\nu(R) \propto R$, the surface density profile $\Sigma(R, t)$ is analytically computed as

$$\Sigma(R, t) = \frac{M_{\rm disk,0}}{2\pi R_1^2}\left(\frac{R}{R_1}\right)^{-1}\left(1 + \frac{t}{t_\nu}\right)^{-3/2} \times \exp\left(-\frac{R}{R_1}\left(1 + \frac{t}{t_\nu}\right)^{-1}\right), \quad \text{(A2)}$$

where $M_{\rm disk,0}$ is the initial disk mass, R_1 is the outer cutoff radius, and $t_\nu \equiv R_1^2/3\nu(R_1)$ is the viscous timescale at R_1. The nominal value of t_ν is

$$t_\nu \sim 0.1\ {\rm Myr}\left(\frac{\alpha}{10^{-3}}\right)^{-1}\left(\frac{M_*}{1\ M_\odot}\right)^{-1/2} \times \left(\frac{H(R_1; M_*, L_*)/R_1}{0.06}\right)^{-2}\left(\frac{R_1}{10\ {\rm au}}\right)^2,$$

with the so-called turbulent α viscosity, $\nu = \alpha\Omega H^2$ (Shakura & Sunyaev 1973). We note that the scale height $H = c_{\rm s}/\Omega$ depends on M_* and L_*; e.g., a passive disk has a temperature profile of

$$T(R, L_*) = T_{\rm eff}\left(\frac{R}{R_*}\right)^{-1/2}\theta_{\rm inc}^{1/4} = \left(\frac{L_*\theta_{\rm inc}}{4\pi\sigma_{\rm SB}R^2}\right)^{1/4},$$

where $\theta_{\rm inc}$ is the incident angle of irradiation, and $\sigma_{\rm SB}$ is the Stefan–Boltzmann constant (Kenyon & Hartmann 1987; Hartmann et al. 1998; Pinilla et al. 2022). The viscous α may also depend on M_* as $\alpha \propto M_*$ so that the accretion rate reproduces the observational scaling profile $\dot{M}_{\rm acc} \propto M_*^2$ (Muzerolle et al. 2003; Calvet et al. 2004; Mohanty et al. 2005; Muzerolle et al. 2005; Natta et al. 2006; Alcalá et al. 2014; Manara et al. 2016; Alcalá et al. 2017; Manara et al. 2022; also see discussions in Gorti et al. 2009 and Kunitomo et al. 2021).

We can calculate the disk mass and mass accretion rate from Equation (A2) as

$$M_{\rm disk}(t) = \int_0^\infty dR\ 2\pi R\Sigma = M_{\rm disk,0}\left(1 + \frac{t}{t_\nu}\right)^{-1/2}, \quad \text{(A3)}$$

$$\dot{M}_{\rm acc} = -\dot{M}_{\rm disk} = \frac{M_{\rm disk,0}}{2t_\nu}\left(1 + \frac{t}{t_\nu}\right)^{-3/2}. \quad \text{(A4)}$$

When photoevaporation is taken into account in Equation (A1), the effect appears on the right-hand side as a sink term:

$$\frac{\partial\Sigma}{\partial t} = \frac{3}{R}\frac{\partial}{\partial R}R^{1/2}\frac{\partial}{\partial R}\nu\Sigma R^{1/2} - \dot{\Sigma}_{\rm ph}.$$

The solution is the so-called UV-switch model (Clarke et al. 2001), and its behavior is described as follows. (1) The disk effectively evolves purely viscously at the early stage. (2) After the accretion rate equals the photoevaporation rate, material supply from the outer part halts. (3) It quickly opens a cavity in the inner region. (4) Photoevaporation dominates mass loss afterward and determines the dispersal time of the remaining disk.

The first transition point at item (2) is when $\dot{M}_{\rm acc}$ is reduced to $\dot{M}_{\rm ph}$. This transition occurs at (using Equation (A4))

$$t_w = t_\nu\left[\left(\frac{M_{\rm disk,0}}{2t_\nu\dot{M}_{\rm ph}}\right)^{2/3} - 1\right] \approx t_\nu\left(\frac{\dot{M}_{\rm acc,0}}{\dot{M}_{\rm ph}}\right)^{2/3} \approx 2.2\ {\rm Myr}\left(\frac{\dot{M}_{\rm acc,0}}{1\times10^{-6}\ M_\odot\ {\rm yr}^{-1}}\right)^{2/3}\left(\frac{\dot{M}_{\rm ph}}{1\times10^{-8}\ M_\odot\ {\rm yr}^{-1}}\right)^{-2/3}, \quad \text{(A5)}$$

where $\dot{M}_{\rm acc,0} \equiv M_{\rm disk,0}/2t_\nu$ is the accretion rate at $t = 0$. By this point, the disk mass has reduced to

$$M'_{\rm disk,0} \equiv M_{\rm disk}(t_w) = M_{\rm disk,0}\left(1 + \frac{t_w}{t_\nu}\right)^{-1/2} = M_{\rm disk,0}\left(\frac{\dot{M}_{\rm acc,0}}{\dot{M}_{\rm ph}}\right)^{-1/3} \approx 0.043\ M_\odot\left(\frac{M_{\rm disk,0}}{0.2\ M_\odot}\right)\left(\frac{\dot{M}_{\rm acc,0}}{10^{-6}\ M_\odot\ {\rm yr}^{-1}}\right)^{-1/3} \times \left(\frac{\dot{M}_{\rm ph}}{10^{-8}\ M_\odot\ {\rm yr}^{-1}}\right)^{1/3}. \quad \text{(A6)}$$

Note that $M_{\rm disk,0}$, t_ν, and $\dot{M}_{\rm acc,0}$ are not independent but are constrained by $M_{\rm disk,0} = 2t_\nu\dot{M}_{\rm acc,0}$.

Material supply from the outer disk stops at $t = t_w$, resulting in a fast draining of the inner region ($R \lesssim 1$ au) on the timescale of the viscous time at the critical radius $R \approx 1$ au, where a gap opens. Photoevaporation governs disk evolution afterward. Note that for disks without the MHD winds' mass loss, t_w and the switching time of our model t_0 are identical. The remaining outer disk disperses by photoevaporation on a timescale of the "initial" outer disk mass $M'_{\rm disk,0}$ over the photoevaporation rate,

$$\frac{M'_{\rm disk,0}}{\dot{M}_{\rm ph}} = 2t_\nu\left(\frac{\dot{M}_{\rm acc,0}}{\dot{M}_{\rm ph}}\right)^{2/3} = 2t_w \approx 4.3\ {\rm Myr}\left(\frac{M_{\rm disk,0}}{0.2\ M_\odot}\right)\left(\frac{\dot{M}_{\rm acc,0}}{10^{-6}\ M_\odot\ {\rm yr}^{-1}}\right)^{-1/3} \times \left(\frac{\dot{M}_{\rm ph}}{10^{-8}\ M_\odot\ {\rm yr}^{-1}}\right)^{-2/3}. \quad \text{(A7)}$$

Hence, the gas disk lifetime is $t_{\rm life,g} = t_w + 2t_w$ in cases of a constant $\dot{M}_{\rm ph}$ before and after t_w.

Photoevaporation rates vary according to stellar evolution, where the luminosities and spectra change by orders of magnitude. Also, if $\dot{M}_{\rm ph}$ gets smaller at some point by, e.g., reduced photoelectric heating due to small-grain depletion, the lifetime is extended. This is the basic idea of our model (and Nakatani et al. 2021) to explain a long-lived gas disk in the context of the primordial-origin scenario.

Appendix B
An Analytic Disk Evolution Model with MHD Effects

The effects of MHD winds are essential in disk evolution. They can remove not only the mass but also the angular momentum of the disk. Chambers (2019) derived an approximate analytic solution for disk evolution with MHD wind

effects. Equation (A1) is modified to

$$\frac{\partial \Sigma}{\partial t} = \frac{3}{R}\frac{\partial}{\partial R}R^{1/2}\frac{\partial}{\partial R}\nu\Sigma R^{1/2} + \frac{1}{R}\frac{\partial}{\partial R}Rv_w\Sigma - \dot{\Sigma}_w, \quad \text{(B1)}$$

where v_w is the inward velocity induced by the disk wind, and $\dot{\Sigma}_w$ is the surface mass-loss rate due to MHD winds. Using a reference radius R_0, the surface mass-loss rate is characterized by a constant parameter K as

$$\dot{\Sigma}_w = -\frac{Kf_w v_0 \Sigma}{R_0}\left(\frac{R}{R_0}\right)^{-3/2}$$
$$K = \frac{1}{2}\left(\frac{R}{R_0}\right)^{-1/4}\left(\frac{\Omega R}{v_{\rm esc} - \Omega R}\right),$$

where v_0 is the inward velocity at R_0, f_w is the fraction of v_0 induced by MHD winds, $v_{\rm esc}$ is the tangential velocity of the winds, and Ω is the Keplerian orbital frequency. The second equation is derived from the conservation of angular momentum.

Chambers (2019) modified Equation (B1) to make it analytically solvable (Equation (12) of the original paper) and found analytic solutions for the modified equation (Equations (36)–(39) of the original paper). We omit writing the solutions explicitly here to avoid complexity and refer the reader to the original paper. The point of this analytic solution is that the surface density and temperature evolution are uniquely determined for a given set of model parameters v_0; f_w; K; the temperature at R_0, T_0; and the surface density at R_0, Σ_0.

For example, $f_w = 0$ means a purely viscous disk, and choosing a high $f_w(\leqslant 1)$ indicates a disk that accretes mainly magnetically. The parameter K can be set to zero with a nonzero f_w. The underlying assumption, in this case, is negligible mass-loss rates due to MHD winds. Small K cases are termed fast wind. On the other hand, using a high value for K ($\leqslant 1$) means that a significant fraction of the accreting gas flows out of the disk before reaching the host star. This case is called a slow wind.

The analytic formula of Chambers (2019) can overall well agree with the true solutions of Equation (B1) regardless of the approximation taken to make the equation analytically tractable. The exception is when the wind mass-loss rate is large; the analytic formula underestimates the surface density and outer spreading at the later stage. It also fails to predict the positive slope of Σ created by the wind in the inner $\sim$1 au region. Nevertheless, the errors between the analytic formula and the true solution are small compared to the large uncertainties in the long-term evolution of disk evolution with the MHD effects. We therefore use the formula as a valid estimate for time-dependent disk mass evolution.

Appendix C
Accretion-generated Emissions

We have omitted accretion-generated UV and X-ray emissions from our model. This extra radiation component can dominate the magnetic and photospheric components, leading to accelerated photoevaporation and reduced $t_{\rm life,g}$. We now examine if this omission affects the study's conclusions—specifically, the peak lifetime beyond 10 Myr at $M_* \approx 2\,M_\odot$ (see Figures 1 and 2). Since the EUV models potentially account for the observed higher occurrence of gas-rich debris disks around A stars, our focus remains exclusively on the EUV models.

The exact portion of accretion luminosity ($L_{\rm acc} \approx GM_*\dot{M}_{\rm acc}/R_*$) contributing to EUV radiation is uncertain. For simplicity, we assume $\sim$4% is processed into EUV emission, aligning with analogous estimation for FUV (Gorti & Hollenbach 2008) and X-ray (Hartmann et al. 2016). This can be represented as

$$\Phi_{\rm EUV,acc} \approx 2 \times 10^{42}\ {\rm s}^{-1}\left(\frac{M_*}{1\,M_\odot}\right)\left(\frac{\dot{M}_{\rm acc}}{10^{-8}\,M_\odot\ {\rm yr}^{-1}}\right)\left(\frac{R_*}{1\,R_\odot}\right)^{-1}.$$

Here, the average EUV photon energy is approximated to match that of 9000 K blackbody radiation, 14.5 eV. The total EUV emission rate is now $\Phi_{\rm EUV} = \Phi_{\rm EUV,ph} + \Phi_{\rm EUV,mag} + \Phi_{\rm EUV,acc}$. In practice, accretion-generated EUV radiation may terminate once the disk develops an inner cavity, when photoevaporation and accretion rates balance at $\sim$1 au (the critical radius for photoevaporation). However, as the cavity-opening time is not determined unambiguously within the framework of our model, we let the accretion-generated EUV emission last until the disk dispersal; this scenario sets the lower limit for $t_{\rm life,g}$.

Figure 4 shows the resulting lifetimes. The accretion-generated EUV dominates $\Phi_{\rm EUV,mag}$ for the weak- and fast-wind disks, especially at the early time ($\lesssim$1 Myr), while laminar disks show minimal total emission rate enhancement. Nevertheless, the photoevaporation rate remains orders of magnitude lower than the accretion and/or MHD wind mass-loss rates at the early stages, with no substantial impact on disk evolution. Except for fast-wind disks, the accretion-generated component becomes negligible as the accretion rate drops in $1\ {\rm Myr} \lesssim t \lesssim 10\ {\rm Myr}$. This occurs prior to the onset of the photoevaporation-dominant epoch at $t = t_0$, leading to minimal shortening of $t_{\rm life,g}$ for the slow-wind and laminar disks.

In contrast, fast-wind disks can maintain relatively high accretion rates ($\sim 10^{-10}$–$10^{-9}\,M_\odot\ {\rm yr}^{-1}$) even at $t = 10$ Myr, with accretion-generated EUV dominating over (or comparable to) the other components throughout dispersal. This impacts $t_{\rm life,g}$ at $M_* = 1.5$–$2.5\,M_\odot$, as $\Phi_{\rm EUV,acc}$ significantly exceeds $\Phi_{\rm EUV,ph} + \Phi_{\rm EUV,mag}$. However, the prevalence of jets and winds observed widely (e.g., Pascucci et al. 2023) suggests that the fast-wind scenario is unlikely to be common among PPDs. It is also difficult to align with the high detection rate of [O I] λ6300 low-velocity components (Nisini et al. 2018). If termination of accretion-generated emissions due to cavity opening is considered, the peak at $M_* \sim 2\,M_\odot$ may remain even for fast-wind disks.

Overall, incorporating the accretion-generated component can moderately reduce $t_{\rm life,g}$ and lessen the stellar mass dependence for disks with no wind mass loss. Nonetheless, not all disks would evolve as fast-wind disks, supporting the highest plausibility of long-living (>10 Myr) gas disks around late intermediate-mass stars. Further investigation is needed to accurately determine $t_{\rm life,g}$, $\Phi_{\rm EUV,acc}$, and its termination time.

Appendix D
Disk Parameter Dependences

We explore how $t_{\rm life,g}$ depends on various disk parameters, including the initial disk mass ($M_{\rm disk,0}$), disk mass scaling law ($M_{\rm disk,0} \propto M_*^{\beta}$), viscous α, and initial disk cutoff radius ($r_{\rm exp}$).

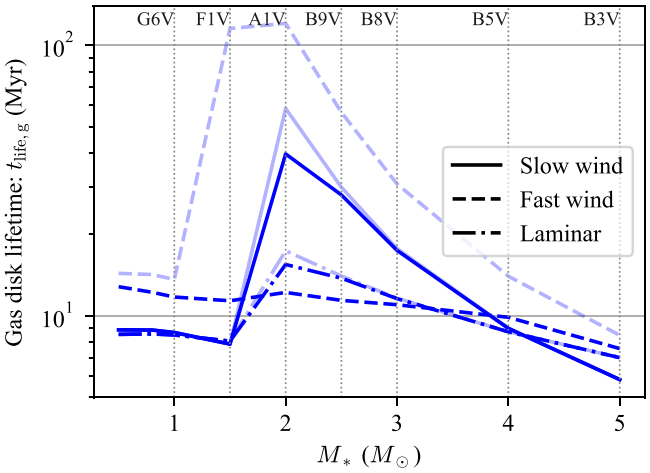

Figure 4. Derived $t_{\rm life,g}$ with accretion-generated EUV (blue). The lifetimes of the fiducial runs are also plotted for comparison (light blue).

These parameters are treated as Monte Carlo variables in population synthesis to span a wide parameter space.

The initial disk mass is defined as $M_{\rm disk,0}/M_* = C_{\rm disk,0}(M_*/1\,M_\odot)^{\beta-1}$, with our fiducial values being $C_{\rm disk,0} = 0.1$ and $\beta = 1$. Exploration covers a range of $0.03 \leqslant C_{\rm disk,0} \leqslant 0.3$ for $C_{\rm disk,0}$ and $1 \leqslant \beta \leqslant 2$, following observations (e.g., Ansdell et al. 2016; Pascucci et al. 2016; Ansdell et al. 2017). As for α, recent findings favor a low value at $10^{-4} \lesssim \alpha \lesssim 10^{-3}$ (Manara et al. 2022), and therefore we vary it in $10^{-4} \leqslant \alpha \leqslant 2 \times 10^{-3}$, with the upper limit encompassing the slow- and fast-wind disks.

The fiducial v_0 values are $30\,{\rm cm\,s^{-1}}$ for slow- and fast-wind disks and $10\,{\rm cm\,s^{-1}}$ for the laminar disk. We explore $10\,{\rm cm\,s^{-1}} \leqslant v_0 \leqslant 30\,{\rm cm\,s^{-1}}$, as values beyond this range lead to unrealistic accretion rate variations. The wind mass-loss parameter K is varied in $0 \leqslant K \leqslant 1$. The initial cutoff radius is tested in 10 au $\leqslant r_{\rm exp} \leqslant$ 40 au; the fiducial is $r_{\rm exp} = 15$ au. For reference, Clarke et al. (2001) and Kunitomo et al. (2020) adopt $r_{\rm exp} = 10$ and 30 au, respectively; the time evolution of the disk radius in the model by Trapman et al. (2022) aligns with the characteristic radii of observed CO disks in Lupus and Upper Sco when $r_{\rm exp} \approx 20$ au and $M_{\rm disk,0} = 0.1\,M_\odot$.

Monte Carlo variables assume uniform densities in linear space, except for $C_{\rm disk,0}$ and α, which follow log-uniform sampling. We perform a total of 90,000 runs: 5000 parameter sets times 9 different stellar masses for each of the EUV and EUV+X-ray models. Figure 5 illustrates the resulting probability densities and cumulative probabilities for $t_{\rm life,g}$, reflecting the trends seen in Figures 1 and 2.

The lifetime is mostly unaffected by β and K. For the EUV and EUV+X-ray models with $M_* \geqslant 3\,M_\odot$, $M_{\rm disk,0}$ has limited influence. However, for EUV+X-ray models with $M_* \leqslant 2.5\,M_\odot$, smaller initial disk masses ($C_{\rm disk,0} \leqslant 0.1$) result in $t_{\rm life,g} \lesssim$ 5 Myr.

Increasing $r_{\rm exp}$ moderately extends $t_{\rm life,g}$. In the EUV models, $t_{\rm life,g}$ tends to exceed 10 Myr for the runs with $M_* \leqslant 1.5\,M_\odot$ and $r_{\rm exp}$(>25 au). Conversely, the most runs with $M_* =$ 2–3 $M_\odot$ and $t_{\rm life,g} < 10$ Myr have $r_{\rm exp} \lesssim 20$ au. When $r_{\rm exp}$ is expanded while keeping $M_{\rm disk,0}$ constant, it decreases the initial surface density in the inner part, leading to greater mass distribution in the outer disk. This leads to slower mass loss via accretion and MHD winds.

Viscous α and v_0 also have a moderate impact on the EUV models, with smaller α and higher v_0 causing shorter lifetimes due to enhanced MHD-driven mass loss and accretion. The longest-$t_{\rm life,g}$ population (>10^2 Myr) at $M_* = 1.5$–$3\,M_\odot$ has $\alpha > 10^{-3}$ and $v_0 < 15\,{\rm cm\,s^{-1}}$, indicating a slow decay of the accretion rate. Unrealistically long lifetimes ($\sim 10^3$ yr) can occur when α is increased to $\sim 10^{-2}$. Hence, when the disk exhibits a characteristic of a viscous disk relatively strongly, $t_{\rm life,g}$ increases significantly.

In summary, higher α and larger $r_{\rm exp}$ can extend $t_{\rm life,g}$ for specific cases. The other parameters exert minor impacts. Regardless of the parameter dependences, overall trends remain consistent. Late intermediate-mass stars in the EUV models consistently exhibit $t_{\rm life,g} > 10$ Myr, peaking at $M_* = 2\,M_\odot$ and declining for lower and higher masses. While the fraction of long-living ($t_{\rm life,g} > 10$ Myr) disks for $M_* \leqslant 1\,M_\odot$, most of which have $r_{\rm exp} > 25$ au, is apparently higher than observations (Figure 3), the actual CO disk lifetime is shorter than $t_{\rm life,g}$. This is because complete CO photodissociation occurs before disk dissipation, when $M_{\rm disk}$ reduces to a certain threshold mass. In addition, X-ray photoevaporation likely causes mass loss at much smaller rates than Equation (3), implying that the lifetimes of the EUV models should be interpreted as upper limits for low-mass stars.

Thermochemistry modeling is needed to interpret these results fully, along with the potentially crucial influence of atypically weak stellar photodissociating fluxes around A stars. It is important to highlight that our findings primarily demonstrate the plausibility of gas disk survival beyond >10 Myr, a necessary condition for supporting the primordial-origin scenario. Additionally, our model qualitatively explains the observed incidence of gaseous debris disks versus stellar mass.

Appendix E
X-Ray Luminosity Spread

Observed X-ray luminosities are known to have a large spread (e.g., Güdel et al. 2007). Accounting for the variability in X-ray luminosity would introduce scattering in the derived lifetimes. In the EUV+X-ray models, amplifying X-ray luminosity results in shorter lifetimes, while reducing it aligns the lifetimes with those of EUV models. Within the EUV models, the spread in luminosity could influence lifetimes for $M_* < 1\,M_\odot$, as their lifetimes are linked to $\Phi_{\rm EUV,mag}$. However, combining Equations (1) and (2), the scaling of EUV photoevaporation rate with $L_{\rm X}^{0.33}$ places a relatively restrained impact on lifetimes. Furthermore, the adopted X-ray luminosity encompasses representative observational values (Figure 6 of Kunitomo et al. 2021). It suggests that derived lifetimes remain relatively stable even when incorporating luminosity spread with a plausible distribution of $L_{\rm X}$. Consequently, the inclusion of luminosity dispersion is unlikely to significantly alter the core finding of this study.

Taking into account the spread of $L_{\rm X}$ along with its time evolution would require solving stellar evolution across a wider parameter space than covered by Kunitomo et al. (2021).

Appendix F
Switching Time and Inner Disk Lifetime

Here, we present the switching time t_0, where photoevaporation begins to dominate over mass-loss rate by accretion and

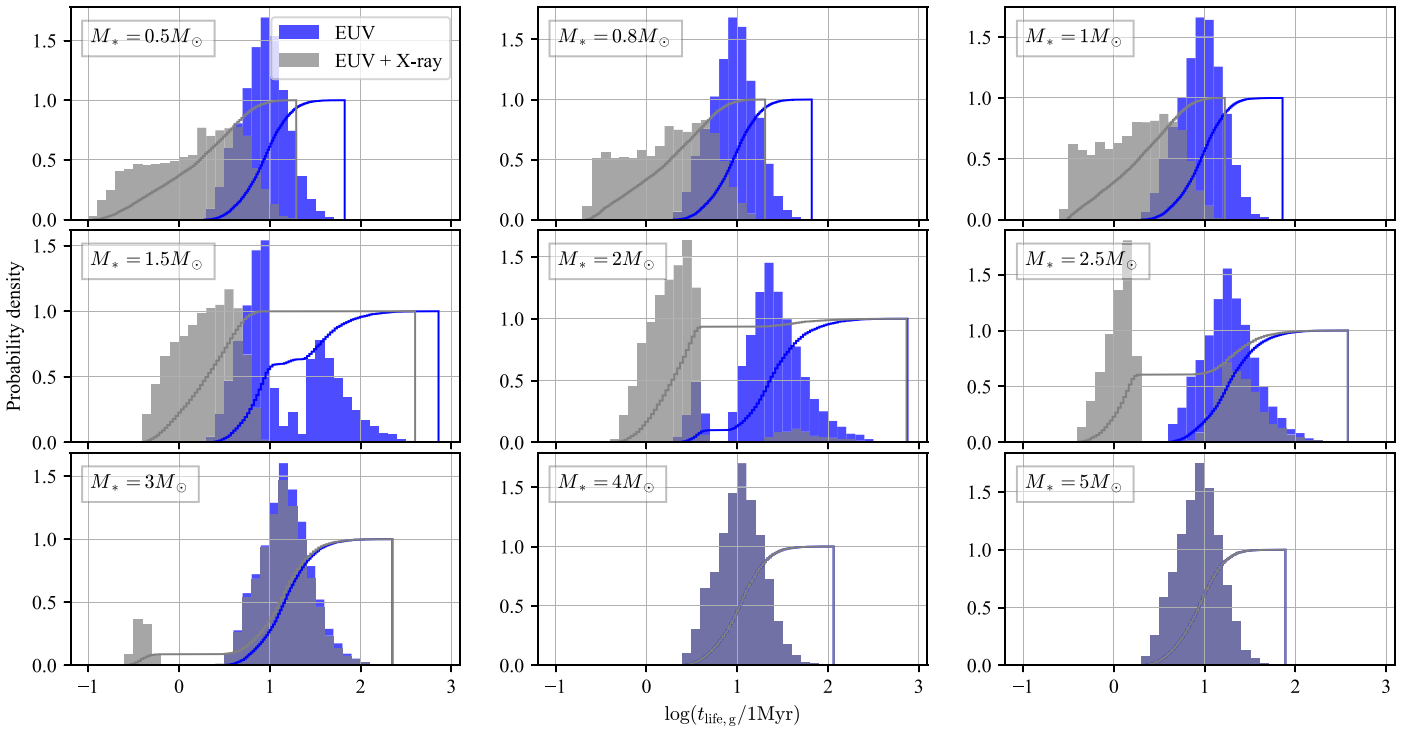

Figure 5. Resulting population. The blue and gray histograms are the probability densities for the EUV and EUV+X-ray models, respectively. Corresponding normalized cumulative probabilities are shown by the solid lines with the same colors.

MHD winds. We also estimate the inner disk lifetimes $t_{\rm w}$, which we assume is the time when the disk opens a cavity by quickly draining the inner disk through accretion. Since our 0D approach cannot determine $t_{\rm w}$ unambiguously, we provide an alternative estimate by identifying the time when the accretion rate at 1 au (the critical radius for photoevaporation) equals the photoevaporation rate. However, we stress that the estimated $t_{\rm w}$ is speculative and carries significant uncertainties. Future 1D models are essential for more meaningful discussions of whether and when the inner cavity opens.

Figure 6 shows t_0, $t_{\rm w}$, and $t_{\rm life,g}$. The ratio $t_0/t_{\rm life,g}$ is typically ∼50%–90%. For the EUV+X-ray models, this ratio is about ∼30%–60% at $M_* < 3\,M_\odot$, except for the laminar disk model with $M_* = 2.5\,M_\odot$, where it is ∼5%. The estimated inner disk lifetime $t_{\rm w}$ is mostly consistent with the observed value (a few megayears; e.g., Fedele et al. 2010) for the EUV models with slow-wind and laminar disks. Note, however, that cluster age determination using the magnetic pre-main-sequence models (Feiden 2016) results in about a factor of 2 longer observational lifetimes (Richert et al. 2018). It is still consistent with the EUV laminar model but somewhat longer than the $t_{\rm w}$ of the EUV slow-wind model. The EUV+X-ray models predict significantly short lifetimes of $t_{\rm w} \lesssim 1$ Myr for $M_* < 3\,M_\odot$. This might result from an overestimation of X-ray photoevaporation rates or suggest the need to incorporate the UV/X-ray shielding due to the accreting flow and disk wind from the inner disk.

In contrast, $t_{\rm w}$ is considerably longer than the observations at $1.5\,M_\odot \leqslant M_* \leqslant 3\,M_\odot$ in the fast-wind EUV models. However, the fast-wind scenario (no wind mass loss while maintaining a high accretion rate for 10 Myr) may not be a major path for PPD evolution, given the high detection rate of the [O I] λ6300 low-velocity component (∼80%; Nisini et al. 2018).

Our model gives a longer t_0 than $t_{\rm w}$ in the slow-wind and laminar models, meaning that wind mass loss continues after the accretion onto the star has weakened. This implies a higher $\dot{M}_{\rm wind}/\dot{M}_{\rm acc}$ than the values of ∼0.1–1 estimated from optical tracers for class II sources (Fang et al. 2018, 2023). The observed ratio is lower still for systems with narrower lines, i.e., winds launched further out (0.5–5 au), which may include disks with inner cavities. However, the actual wind mass-loss rates could be higher, as the optical lines trace only atomic winds. An indication is the object HH 30, where slow molecular winds are detected in CO with a mass-loss rate of $\gtrsim 9 \times 10^{-8}\,M_\odot\,{\rm yr}^{-1}$ (Louvet et al. 2018), yielding $\dot{M}_{\rm wind}/\dot{M}_{\rm acc} \sim 5$, which is comparable to the values estimated for magnetocentrifugal winds (∼2.3; Hasegawa et al. 2022). Overall, it is currently unclear whether PPDs go into a high $\dot{M}_{\rm wind}/\dot{M}_{\rm acc}$ mode like that indicated by some of the models here. This will be addressed in the near future through ALMA observations of cold, slow molecular winds.

We reiterate that our $t_{\rm w}$ estimate is quite uncertain over when and whether the inner cavity opens and remains open after the host star's convection dies away. A more meaningful comparison will necessitate evaluating surface mass-loss and accretion rates at individual radii through 1D radial modeling. This will help determine whether the long outer disk lifetimes proposed in this study are compatible with observational constraints on stellar accretion and winds. Considering the uncertainties, the main conclusions to draw from the calculations presented in this Appendix are that (1) the EUV+X-ray models are disfavored, since the high X-ray photoevaporation rates yield too-short inner disk lifetimes, and (2) the fast-wind scenario is unlikely, since slow winds are commonly observed.

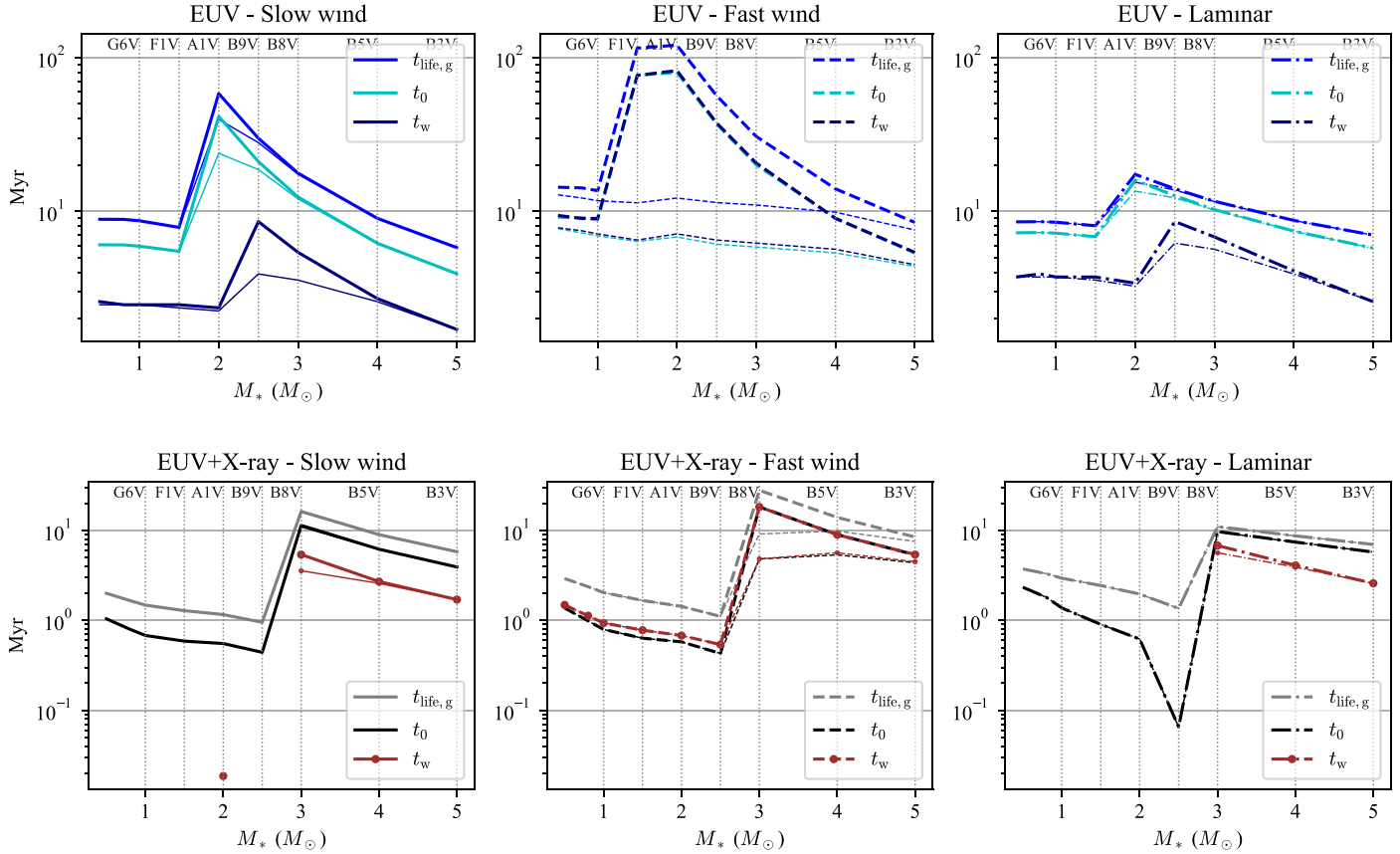

Figure 6. Gas lifetime ($t_{\rm life,g}$), switching time (t_0), and estimated inner gas disk lifetime ($t_{\rm w}$) for the EUV (top) and EUV+X-ray (bottom) models with slow-wind, fast-wind, and laminar disks. Thicker lines represent scenarios excluding accretion-generated EUV (Appendix C), while thinner lines depict those with it. In the bottom left and right panels, $t_{\rm w}$ is omitted for $M_* < 3\,M_\odot$, except for $M_* = 2\,M_\odot$ in the bottom left panel, since $t_{\rm w}$ is not found in $t > 0.01$ Myr. In the middle panels (fast-wind disks), the lines for t_0 and $t_{\rm w}$ almost overlap.

ORCID iDs

Riouhei Nakatani https://orcid.org/0000-0002-1803-0203
Neal J. Turner https://orcid.org/0000-0001-8292-1943
Gianni Cataldi https://orcid.org/0000-0002-2700-9676
Yuri Aikawa https://orcid.org/0000-0003-3283-6884
Sebastián Marino https://orcid.org/0000-0002-5352-2924

References

Acke, B., Bouwman, J., Juhász, A., et al. 2010, ApJ, 718, 558
Alcalá, J. M., Manara, C. F., Natta, A., et al. 2017, A&A, 600, A20
Alcalá, J. M., Natta, A., Manara, C. F., et al. 2014, A&A, 561, A2
Alexander, R., Rosotti, G., Armitage, P. J., et al. 2023, NRAS, 524, 3948
Andrews, S. M., Rosenfeld, K. A., Kraus, A. L., & Wilner, D. J. 2013, ApJ, 771, 129
Ansdell, M., Williams, J. P., Manara, C. F., et al. 2017, AJ, 153, 240
Ansdell, M., Williams, J. P., van der Marel, N., et al. 2016, ApJ, 828, 46
Astropy Collaboration, Price-Whelan, A. M., Lim, P. L., et al. 2022, ApJ, 935, 167
Astropy Collaboration, Price-Whelan, A. M., Sipőcz, B. M., et al. 2018, AJ, 156, 123
Astropy Collaboration, Robitaille, T. P., Tollerud, E. J., et al. 2013, A&A, 558, A33
Bai, X.-N., & Stone, J. M. 2013a, ApJ, 767, 30
Bai, X.-N., & Stone, J. M. 2013b, ApJ, 769, 76
Calvet, N., Muzerolle, J., Briceño, C., et al. 2004, AJ, 128, 1294
Carrera, D., Gorti, U., Johansen, A., & Davies, M. B. 2017, ApJ, 839, 16
Cataldi, G., Aikawa, Y., Iwasaki, K., et al. 2023, ApJ, 951, 111
Cataldi, G., Wu, Y., Brandeker, A., et al. 2020, ApJ, 892, 99
Chambers, J. 2019, ApJ, 879, 98
Clarke, C. J., Gendrin, A., & Sotomayor, M. 2001, MNRAS, 328, 485
Dent, W. R. F., Wyatt, M. C., Roberge, A., et al. 2014, Sci, 343, 1490
Ercolano, B., Clarke, C. J., & Drake, J. J. 2009, ApJ, 699, 1639
Fang, M., Pascucci, I., Edwards, S., et al. 2018, ApJ, 868, 28
Fang, M., Pascucci, I., Edwards, S., et al. 2023, ApJ, 945, 112
Fedele, D., van den Ancker, M. E., Henning, T., Jayawardhana, R., & Oliveira, J. M. 2010, A&A, 510, A72
Feiden, G. A. 2016, A&A, 593, A99
Furlan, E., Hartmann, L., Calvet, N., et al. 2006, ApJS, 165, 568
Furlan, E., Luhman, K. L., Espaillat, C., et al. 2011, ApJS, 195, 3
Geers, V. C., Augereau, J. C., Pontoppidan, K. M., et al. 2006, A&A, 459, 545
Geers, V. C., van Dishoeck, E. F., Visser, R., et al. 2007, A&A, 476, 279
Gorti, U., Dullemond, C. P., & Hollenbach, D. 2009, ApJ, 705, 1237
Gorti, U., & Hollenbach, D. 2008, ApJ, 683, 287
Gorti, U., Hollenbach, D., & Dullemond, C. P. 2015, ApJ, 804, 29
Greaves, J. S., Holland, W. S., Matthews, B. C., et al. 2016, MNRAS, 461, 3910
Güdel, M., Briggs, K. R., Arzner, K., et al. 2007, A&A, 468, 353
Haisch, K. E., Jr+, Lada, E. A., & Lada, C. J. 2001, ApJL, 553, L153
Hamaguchi, K., Yamauchi, S., & Koyama, K. 2005, ApJ, 618, 360
Harris, C. R., Millman, K. J., van der Walt, S. J., et al. 2020, Natur, 585, 357
Hartmann, L., Calvet, N., Gullbring, E., & D'Alessio, P. 1998, ApJ, 495, 385
Hartmann, L., Herczeg, G., & Calvet, N. 2016, ARA&A, 54, 135
Hasegawa, Y., Haworth, T. J., Hoadley, K., et al. 2022, ApJL, 926, L23
Hernández, J., Hartmann, L., Megeath, T., et al. 2007, ApJ, 662, 1067
Higuchi, A. E., Oya, Y., & Yamamoto, S. 2019a, ApJL, 885, L39
Higuchi, A. E., Saigo, K., Kobayashi, H., et al. 2019b, ApJ, 883, 180
Higuchi, A. E., Sato, A., Tsukagoshi, T., et al. 2017, ApJL, 839, L14
Hollenbach, D., Johnstone, D., Lizano, S., & Shu, F. 1994, ApJ, 428, 654
Hughes, A. M., Duchêne, G., & Matthews, B. C. 2018, ARA&A, 56, 541
Hughes, A. M., Lieman-Sifry, J., Flaherty, K. M., et al. 2017, ApJ, 839, 86
Hunter, J. D. 2007, CSE, 9, 90
Iglesias, D. P., Panić, O., van den Ancker, M., et al. 2023, MNRAS, 519, 3958
Iwasaki, K., Kobayashi, H., Higuchi, A. E., & Aikawa, Y. 2023, ApJ, 950, 36
Johnston, H., Panic, O., & Liu, B. 2023, MNRAS, 527, 2303
Kennedy, G. M., & Kenyon, S. J. 2009, ApJ, 695, 1210
Kenyon, S. J., & Hartmann, L. 1987, ApJ, 323, 714

Komaki, A., Fukuhara, S., Suzuki, T. K., & Yoshida, N. 2023, arXiv:2304.13316
Komaki, A., Nakatani, R., & Yoshida, N. 2021, ApJ, 910, 51
Kóspál, Á., Moór, A., Juhász, A., et al. 2013, ApJ, 776, 77
Kral, Q., Marino, S., Wyatt, M. C., Kama, M., & Matrà, L. 2019, MNRAS, 489, 3670
Kral, Q., Matrà, L., Kennedy, G. M., Marino, S., & Wyatt, M. C. 2020, MNRAS, 497, 2811
Kral, Q., Wyatt, M., Carswell, R. F., et al. 2016, MNRAS, 461, 845
Kunitomo, M., Ida, S., Takeuchi, T., et al. 2021, ApJ, 909, 109
Kunitomo, M., Suzuki, T. K., & Inutsuka, S.-i. 2020, MNRAS, 492, 3849
Li, A., & Lunine, J. I. 2003, ApJ, 594, 987
Lieman-Sifry, J., Hughes, A. M., Carpenter, J. M., et al. 2016, ApJ, 828, 25
Louvet, F., Dougados, C., Cabrit, S., et al. 2018, A&A, 618, A120
Lynden-Bell, D., & Pringle, J. E. 1974, MNRAS, 168, 603
Mamajek, E. E. 2009, in AIP Conf. Ser. 1158, ed. T. Usuda, M. Tamura, & M. Ishii (Melville, NY: AIP), 3
Manara, C. F., Ansdell, M., Rosotti, G. P., et al. 2022, in ASP Conf. Series 534, Protostars and Planets VII, ed. S. Inutsuka et al. (San Francisco, CA: ASP), 539
Manara, C. F., Fedele, D., Herczeg, G. J., & Teixeira, P. S. 2016, A&A, 585, A136
Mangeney, A., & Praderie, F. 1984, A&A, 130, 143
Marino, S., Cataldi, G., Jankovic, M. R., Matrà, L., & Wyatt, M. C. 2022, MNRAS, 515, 507
Marino, S., Flock, M., Henning, T., et al. 2020, MNRAS, 492, 4409
Marino, S., Matrà, L., Stark, C., et al. 2016, MNRAS, 460, 2933
Matrà, L., Öberg, K. I., Wilner, D. J., Olofsson, J., & Bayo, A. 2019, AJ, 157, 117
Meyer, M. R., Backman, D. E., Weinberger, A. J., & Wyatt, M. C. 2007, in Protostars and Planets V, 951, ed. B. Reipurth, D. Jewitt, & K. Keil (Tucson, AZ: Univ. of Arizona Press), 573
Mohanty, S., Jayawardhana, R., & Basri, G. 2005, ApJ, 626, 498
Moór, A., Curé, M., Kóspál, Á., et al. 2017, ApJ, 849, 123
Moór, A., Kral, Q., Ábrahám, P., et al. 2019, ApJ, 884, 108
Mulders, G. D., Min, M., Dominik, C., Debes, J. H., & Schneider, G. 2013, A&A, 549, A112
Muzerolle, J., Hillenbrand, L., Calvet, N., Briceño, C., & Hartmann, L. 2003, ApJ, 592, 266
Muzerolle, J., Luhman, K. L., Briceño, C., Hartmann, L., & Calvet, N. 2005, ApJ, 625, 906
Nakatani, R., Hosokawa, T., Yoshida, N., Nomura, H., & Kuiper, R. 2018a, ApJ, 857, 57
Nakatani, R., Hosokawa, T., Yoshida, N., Nomura, H., & Kuiper, R. 2018b, ApJ, 865, 75
Nakatani, R., Kobayashi, H., Kuiper, R., Nomura, H., & Aikawa, Y. 2021, ApJ, 915, 90
Natta, A., Testi, L., & Randich, S. 2006, A&A, 452, 245
Nisini, B., Antoniucci, S., Alcalá, J. M., et al. 2018, A&A, 609, A87
Noyes, R. W., Hartmann, L. W., Baliunas, S. L., Duncan, D. K., & Vaughan, A. H. 1984, ApJ, 279, 763
Oliveira, I., Pontoppidan, K. M., Merín, B., et al. 2010, ApJ, 714, 778
Owen, J. E., Clarke, C. J., & Ercolano, B. 2012, MNRAS, 422, 1880
Owen, J. E., Ercolano, B., & Clarke, C. J. 2011, MNRAS, 412, 13
Owen, J. E., Ercolano, B., Clarke, C. J., & Alexander, R. D. 2010, MNRAS, 401, 1415
Owen, J. E., & Kollmeier, J. A. 2019, MNRAS, 487, 3702
Pascucci, I., Banzatti, A., Gorti, U., et al. 2020, ApJ, 903, 78
Pascucci, I., Cabrit, S., Edwards, S., et al. 2023, in ASP Conf. Ser. 534, Protostars and Planets VII, ed. S.-i. Inutsuka et al. (San Francisco, CA: ASP), 567
Pascucci, I., Testi, L., Herczeg, G. J., et al. 2016, ApJ, 831, 125
Pecaut, M. J., & Mamajek, E. E. 2013, ApJS, 208, 9
Picogna, G., Ercolano, B., Owen, J. E., & Weber, M. L. 2019, MNRAS, 487, 691
Pinilla, P., Garufi, A., & Gárate, M. 2022, A&A, 662, L8
Potravnov, I. S., Eselevich, M. V., Kondratieva, T. E., & Sokolov, I. V. 2018, AstL, 44, 603
Ribas, Á., Bouy, H., & Merín, B. 2015, A&A, 576, A52
Rab, C., Weber, M., Grassi, T., et al. 2022, A&A, 668, A154
Rafikov, R. R. 2017, ApJ, 837, 163
Reffert, S., Bergmann, C., Quirrenbach, A., Trifonov, T., & Künstler, A. 2015, A&A, 574, A116
Ribas, Á., Merín, B., Bouy, H., & Maud, L. T. 2014, A&A, 561, A54
Richert, A. J. W., Getman, K. V., Feigelson, E. D., et al. 2018, MNRAS, 477, 5191
Richling, S., & Yorke, H. W. 1998, A&A, 340, 508
Ronco, M. P., Schreiber, M. R., Villaver, E., Guilera, O. M., & Miller Bertolami, M. M. 2023, arXiv:2311.03934
Sellek, A. D., Booth, R. A., & Clarke, C. J. 2020, MNRAS, 498, 2845
Sellek, A. D., Clarke, C. J., & Ercolano, B. 2022, MNRAS, 514, 535
Shakura, N. I., & Sunyaev, R. A. 1973, A&A, 24, 337
Shoda, M., & Takasao, S. 2021, A&A, 656, A111
Shu, F. H., Johnstone, D., & Hollenbach, D. 1993, Icar, 106, 92
Sicilia-Aguilar, A., Henning, T., & Hartmann, L. W. 2010, ApJ, 710, 597
Smirnov-Pinchukov, G. V., Moór, A., Semenov, D. A., et al. 2022, MNRAS, 510, 1148
Stelzer, B., Micela, G., Hamaguchi, K., & Schmitt, J. H. M. M. 2006, A&A, 457, 223
Su, K. Y. L., Kennedy, G. M., Schlawin, E., Jackson, A. P., & Rieke, G. H. 2022, ApJ, 927, 135
Suzuki, T. K., & Inutsuka, S.-i 2009, ApJL, 691, L49
Takasao, S., Tomida, K., Iwasaki, K., & Suzuki, T. K. 2022, ApJ, 941, 73
Tanaka, K. E. I., Nakamoto, T., & Omukai, K. 2013, ApJ, 773, 155
Thi, W. F., Pinte, C., Pantin, E., et al. 2014, A&A, 561, A50
Trapman, L., Tabone, B., Rosotti, G., & Zhang, K. 2022, ApJ, 926, 61
van der Marel, N., & Mulders, G. D. 2021, AJ, 162, 28
Vicente, S., Berné, O., Tielens, A. G. G. M., et al. 2013, ApJL, 765, L38
Virtanen, P., Gommers, R., Oliphant, T. E., et al. 2020, NatMe, 17, 261
Wang, L., & Goodman, J. 2017, ApJ, 847, 11
Weber, M. L., Ercolano, B., Picogna, G., Hartmann, L., & Rodenkirch, P. J. 2020, MNRAS, 496, 223
Weder, J., Mordasini, C., & Emsenhuber, A. 2023, A&A, 674, A165
Williams, J. P., & Cieza, L. A. 2011, ARA&A, 49, 67
Wolthoff, V., Reffert, S., Quirrenbach, A., et al. 2022, A&A, 661, A63